Developments in the Built Environment 17 (2024) 100351

Contents lists available at ScienceDirect

Developments in the Built Environment

journal homepage: www.sciencedirect.com/journal/developments-in-the-built-environment

Carbonate biomineralization potential of endospore-laden polymeric fibers (BioFibers) for bio-self-healing applications

Mohammad Houshmand Khaneghahi [a,*], Seyed Ali Rahmaninezhad [a], Divya Kamireddi [b], Amirreza Sadighi [c], Christopher M. Sales [a], Caroline L. Schauer [b], Ahmad Najafi [c], Yaghoob (Amir) Farnam [a]

[a] Department of Civil, Architectural, and Environmental Engineering, Drexel University, Philadelphia, PA, USA
[b] Department of Materials Science and Engineering, Drexel University, Philadelphia, PA, USA
[c] Department of Mechanical Engineering and Mechanics, Drexel University, Philadelphia, PA, USA

ARTICLE INFO

Keywords:
Calcium carbonate
Crystal structure
Endospore
Material characterization
Polymorphs
Self-healing

ABSTRACT

This study explores the capacity and kinetics of microbially-induced calcium carbonate precipitation (MICCP) using BioFibers—endospore-laden polymeric fibers. Innovatively developed as a delivery system, BioFibers incorporate a bio-self-healing feature into quasi-brittle composites like concrete. Constructed with a load-bearing core fiber, a bio-compatible hydrogel sheath, and an outer protective shell layer, BioFibers represent a novel approach to enhancing material healing properties. BioFibers have been engineered to provide the matrix with three functionalities: autonomous self-healing, crack growth control, and damage-induced activation. The primary goal of this study was to focus on the self-healing functionality of BioFibers and evaluate the biomineralization performance through advanced material characterization techniques. In this context, we conducted quantitative and qualitative experiments to study bio-self-healing kinetics and precipitates material characterizations using thermogravimetric analysis (TGA), scanning electron microscopy equipped with energy-dispersive spectroscopy (SEM-EDS) and X-ray powder diffraction (XRD). TGA results revealed that the self-healing kinetics based on calcium carbonate precipitation were mainly exhibited by three stages: (i) endospore germination lag phase, (ii) ureolytic activity, and (iii) saturation degree of carbonate, resulting in precipitations of calcium carbonate per one activated BioFiber (with an average mass of 56.9 ± 1.4 mg) equal to: (i) 3.35–30.30 mg, (ii) 31.08–140.91 mg, and (iii) 381.39–620.08 mg, respectively. SEM imaging revealed growing calcium carbonate crystal formation, primarily vaterite, during the progression of MICCP. EDS data in the initial stage indicated traces of phosphorus, potassium, nitrogen, sodium, and sulfur, signaling the endospore germination phase. In subsequent stages, carbon, calcium, and oxygen elements dominated, confirming calcium carbonate precipitation. XRD phase analysis showed that amorphous content was the primary residue in the first stage, with 85.5% associated with organic matter and 5.6 wt% due to amorphous calcium carbonate. As the MICCP process continued, the amorphous content, mainly organic matter, decreased, reaching 23.5 wt% in the last stage. Conversely, the crystalline phase increased, with calcite accounting for 21.4 wt% and vaterite accounting for 51.7 wt% in the final stage.

1. Introduction

Bio self-healing materials have gained significant attention for their potential to revolutionize industries like aerospace, automotive, construction, and healthcare (Daminabo et al., 2020; El Falafli and Hassan, 2021; Raina et al., 2021). These materials mimic biological systems by autonomously repairing themselves upon damage occurrence (Toohey et al., 2007; Vijayan and Puglia, 2019). By incorporating self-healing mechanisms, the materials can recover their mechanical and/or chemical properties (Ghosh, 2009). This ability to heal not only extends product lifespan and durability but also reduces maintenance costs, increases reliability, and promotes sustainability by minimizing waste and optimizing resource utilization (Chen et al., 2023). Ongoing research in this field aims to develop materials with enhanced resilience and

* Corresponding author.
E-mail address: mhk58@drexel.edu (M. Houshmand Khaneghahi).

https://doi.org/10.1016/j.dibe.2024.100351
Received 19 October 2023; Received in revised form 13 January 2024; Accepted 26 January 2024
Available online 5 February 2024

functionality (Bekas et al., 2016; Guimard et al., 2012). A promising area of research in bio-self-healing focuses on utilizing microbially-induced calcium carbonate precipitation (MICCP) as a healing agent for quasi-brittle materials since calcium carbonate is a compatible repairing mineral with quasi-brittle materials. This substance shows potential for repairing and filling cracks or fractures (Amran et al., 2022; Sohail et al., 2022). Calcium carbonate holds great promise for self-healing applications in various fields, including biomedical implants, ceramics, construction materials, and most importantly cementitious composites (e.g., concrete) (Wang et al., 2021). Calcium carbonate demonstrates excellent compatibility with biological systems, making it suitable for integration into materials that interact with such systems (Nguyen et al., 2018). Moreover, its compatibility with cementitious composites ensures that it does not compromise the overall mechanical properties of the materials (L. Li et al., 2019). By implementing engineered self-healing mechanisms, the deposition of calcium carbonate into cracks can effectively seal and restore the structural integrity of the material (Wenting Li et al., 2018).

Calcium carbonate can be precipitated biologically through different pathways such as metabolic/microbial pathways and extracellular matrix production (Manzo et al., 2013; Shrestha et al., 2022). In metabolic/microbial pathways, microorganisms, including bacteria, archaea, and fungi, can actively control the precipitation of calcium carbonate (Martin et al., 2012). These microorganisms can produce enzymes or metabolic byproducts that affect the local chemical environment, leading to the precipitation of calcium carbonate (Hoffmann et al., 2021; Siddique and Chahal, 2011). In addition, these microorganism act as templates or nucleation sites, guiding the growth and arrangement of calcium carbonate crystals (Nawarathna et al., 2019; Simon et al., 2022). In extracellular matrix production, certain organisms, such as corals, algae, or mollusks, secrete an extracellular matrix composed of organic materials (Weiner and Dove, 2003). This matrix provides a scaffold or framework for the deposition of calcium carbonate crystals (Szcześ et al., 2018). The organisms can control the composition and structure of the matrix to influence the formation of calcium carbonate (Azulay et al., 2018). In the context of the MICCP process, urea hydrolysis has emerged as the one of the most effective mechanisms for promoting concrete self-healing (Castro-Alonso et al., 2019; Gebru et al., 2021; Xu et al., 2018). The principle of MICP technology involves catalyzing urea hydrolysis by secreting urease through ureolytic bacteria, leading to the discharge of hydroxide and ammonium ions (Qin et al., 2021). In the case of using dormant bacteria, i.e., endospores, for ureolytic-driven MICCP process, when favorable growth conditions are sensed by endospores, the germination phase is triggered, leading to outgrowth and the production of vegetative cells (S. A. Rahmaninezhad, A. Y. Farnam, C. L. Schauer, A. Raeisi Najafi, & C. M. Sales, 2022a; S. A. Rahmaninezhad, Y. A. Farnam, C. L. Schauer, A. Raeisi Najafi, & C. M. Sales, 2022b). Then, carbonate ion (CO_3^{2-}) production based on hydrolysis of urea (CH_4N_2O) occurred and progressed over time (Castro-Alonso et al., 2019). The urea hydrolysis-driven MICCP generally involved the reactions described in the following (Seifan et al., 2020):

$$CH_4N_2O + H_2O \rightarrow NH_2COOH + NH_3 \quad \text{Eq. 1}$$

$$NH_2COOH + H_2O \rightarrow NH_3 + H_2CO_3 \quad \text{Eq. 2}$$

$$2NH_3 + 2H_2O \leftrightarrow 2NH_4^+ + 2OH^- \quad \text{Eq. 3}$$

$$H_2CO_3 \leftrightarrow HCO_3^- + H^+ \quad \text{Eq. 4}$$

$$HCO_3^- + H^+ + 2OH^- \leftrightarrow CO_3^{2-} + 2H_2O \quad \text{Eq. 5}$$

$$CO_3^{2-} + Ca^{2+} \rightarrow CaCO_3 \quad \text{Eq. 6}$$

Germinated vegetative cells generate urease to catalyze the breakdown of urea into ammonia (NH_3) and soluble carbamic acid (NH_2COOH) through hydrolysis (Preetham et al., 2021; Seifan et al., 2020). Furthermore, the presence of a negatively charged cell surface facilitates the formation of nucleation sites, which promotes the precipitation of calcium carbonate (Ortega-Villamagua et al., 2020).

MICCP can result in the formation of calcium carbonate in different forms, including calcite, aragonite, vaterite, and an amorphous phase (Dhami et al., 2013). These polymorphs of calcium carbonate exhibit variations in crystal structure, stability, solubility, and physical properties (Vidallon et al., 2020). The formation of different calcium carbonate polymorphs during MICCP is influenced by a range of factors, such as biological control, environmental conditions, and the kinetics of mineral precipitation (Dhami et al., 2013; L. V. Zhang et al., 2021). Each microorganism may employ distinct biological mechanisms that promote the formation of specific polymorphs (Wei Li et al., 2010). Additionally, environmental factors like temperature, pressure, pH, and the availability of ions and nutrients can impact the stability and formation rate of different polymorphs (MacAdam and Jarvis, 2015). The rate at which nucleation and crystal growth occur can also affect the crystallization process of calcium carbonate polymorphs (Mitchell and Ferris, 2006). Different polymorphs of calcium carbonate possess distinct physical and chemical attributes that make them suitable for diverse applications (Jimoh et al., 2018; Saulat et al., 2020). Calcite, the most stable and least soluble form, is widely used in the construction industry, building materials, and cement production (Anbu et al., 2016; Dhami et al., 2013; Thenepalli et al., 2015). Aragonite, another prevalent form, finds application as a biomaterial for repairing fractured bones, developing advanced drug delivery systems, and constructing tissue scaffolds (Macha and Ben-Nissan, 2018; Muhammad Mailafiya et al., 2019). Vaterite, although less stable, has valuable roles in the biomedical and pharmaceutical sectors, acting as a carrier for drug delivery systems and aiding tissue engineering and biomineralization research (Maleki Dizaj et al., 2019; Zafar et al., 2022).

Previously, we investigated the feasibility of developing BioFibers with the capability of producing calcium carbonate as self-healing end-product (Khaneghahi et al., 2023a, 2023c). These BioFibers have been created using polyvinyl alcohol (PVA) as a core-fiber, a sheath of crosslinked alginate as a carrier for bacterial endospore, and an outer impermeable layer of polystyrene and polylactic acid copolymer blends. The primary functionality of BioFibers was to serve as a delivery method for bio-self-healing agent, i.e., bacterial endospore, into the desired quasi-brittle matrix (e.g., cementitious matrix). The self-healing process in BioFiber-reinforced concrete, depicted in Fig. 1, initiates with the ingress of aqueous solution from environment into the crack volume and partially fractured BioFiber, followed by swollen alginate to distribute and release endospores into crack volume. In the presence of nutrients, urea and calcium from the matrix, therefore, MICP self-activation occurs, and accordingly, calcium carbonate polymorphs are deposited into the cracked area, effectively filling and sealing the cracks. The BioFibers novel functionalities include: autonomous self-healing, crack growth control, and damage-induced activation (Khaneghahi et al., 2023a).

The primary advantage of BioFiber as a bio-agent carrier over other delivery methods, including encapsulation, is its ability to introduce crack growth control capability into concrete. Cultivated through meticulous design, BioFiber features a core fiber that not only creates a crack bridging effect but also aims to elevate the fracture and mechanical properties of concrete structures. Furthermore, BioFiber holds a distinct advantage over vascular networks, which are used as self-healing channels inside concrete, due to its simplified integration into concrete structures during concrete casting. This effective incorporation provides a damage-responsive self-healing attribute, avoiding adverse effects and simultaneously enhancing the mechanical and fracture properties of the matrix. Moreover, a damage-induced healing activation mechanism has been integrated into BioFibers by adding a strain-responsive polymeric-based shell coating. The shell layer is designed to withstand the concrete casting process without experiencing any fractures or unwanted release of bio-agents, breaking only upon concrete cracking reaching each BioFiber. In the selection of the shell

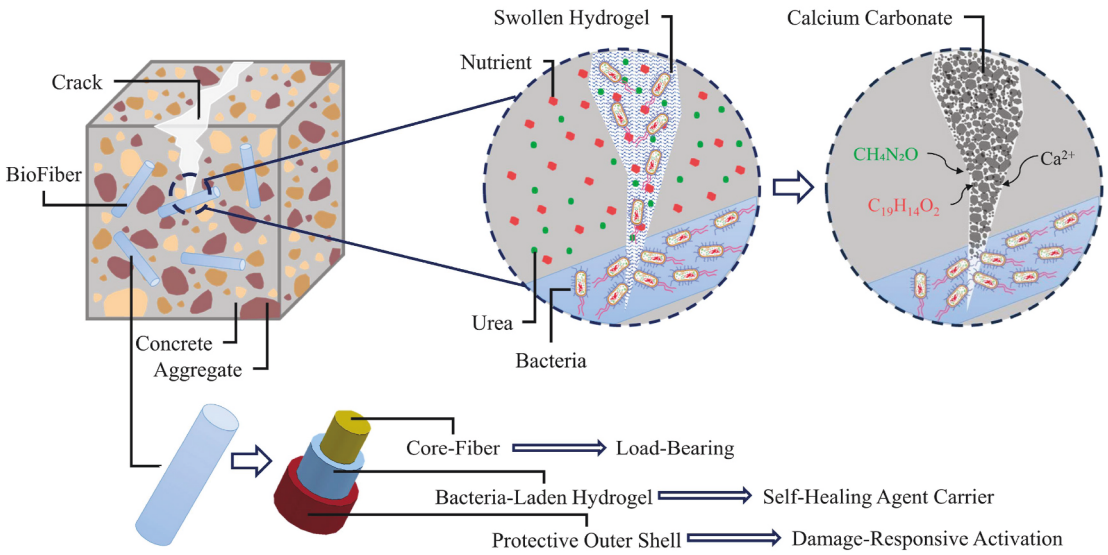

Fig. 1. Schematic illustration of activated BioFiber and its component in cementitious matrix.

material, different material mismatch cases for the critical energy release rate of the shell, compared to that of the core fiber and matrix, have been investigated using a phase-field fracture framework (Sadighi et al., 2023).

In the present study, we investigated self-healing kinetics, particularly within the realm of biological systems, and characterized the minerals formed as the ultimate products of self-healing. Understanding self-healing kinetics is essential for comprehending the full potential of innovative BioFibers in sealing, filling, and healing damage-induced cracks in materials, especially those prone to microcrack formations such as quasi-brittle composites. The exploration of self-healing kinetics and capacity has significant potential for engineering biomimetic materials with self-healing capabilities for diverse applications. To achieve this goal, we devised an experimental design incorporating: (i) thermogravimetric analysis to quantify precipitation kinetics, (ii) microstructural and elemental analysis to examine the morphology of precipitates, and (iii) crystal structure analysis to conduct phase quantification on the calcium carbonate polymorphs, i.e., the end-products of self-healing.

2. Materials and methods

2.1. BioFiber production

The BioFibers were developed using three primary components as: (i) core-fiber, (ii) biocompatible hydrogel coating, and (iii) protective outer layer (Khaneghahi et al., 2023a, 2023c). The core-fiber acts as a load-bearing rigid element for the BioFibers made with insoluble polyvinyl alcohol (PVA) fibers. These fibers are monofilaments with an average length and diameter of 30 mm and 611 μm, respectively. In terms of mechanical properties, the core-fibers have a tensile strength of 800 MPa and elastic modulus of 23 GPa. The hydrogel coating was created by using sodium-alginate (Sigma-Aldrich, CAS: 9005-38-3, MW of 12,000–80,000 g/mol) crosslinked with calcium acetate solution (MP Biomedicals, CAS: 5743-26-0). The concentration of the sodium-alginate solution has been adjusted considering (i) the desired morphology of the coating layer with low coating-to-fiber ratio and uniformity, and (ii) the hydrogel swelling capacity. Previous studies have demonstrated that using an 8 w/v sodium-alginate solution in conjunction with a 0.259 M calcium acetate solution yielded favorable outcomes in meeting the criteria of uniform coating and high swelling capacity (Khaneghahi et al., 2023b).

The *Lysinibacillus sphaericus* strain MB284 endospores solution, as self-healing agents, was blended with sodium-alginate solution prior to crosslinking phase. The bacterial strain was cultivated in a medium comprising distilled water, peptone, beef extract (10 g/L each), and sodium chloride (5 g/L) to revive the strain. The pH of the culture medium was adjusted to 7 using a phosphate-buffered saline (PBS) solution. Preceding cell inoculation, the culture medium underwent autoclaving at 121 °C for 15 min, then, incubated in the specified culture medium within a shaker incubator at 35 °C and 150 rpm for one day. Upon reaching an OD_{600} (optical density at a wavelength of 600 nm) of ~1, 25 ml of the culture medium was transferred to 50 ml conical polypropylene centrifuge tubes. The sample underwent centrifugation for 10 min at 7830 rpm and 25 °C to separate the solid phase containing cells from the supernatant. The bacterial strains were then washed three times with a PBS solution before being introduced into a fresh PBS solution. The pour-plate technique was utilized to determine cell concentration, revealing that the bacterial strain attained a concentration of 10^9 cells/ml, i.e., as $OD_{600} = 1$, (Rahmaninezhad et al., 2022a, 2022b). The endospores were prepared via thermal shock endosporulation method. Employing the thermal shock method, the vegetative cells underwent three washes with a 1 M (PBS before being introduced into Minimal Salt Media (MSM), recipe can be found in (Rahmaninezhad et al., 2022b). In the subsequent phase, the cells were subjected to a 30-min incubation in a boiling water bath, followed by an additional 30 min in an ice water bath—a process known as the thermal shock endosporulation method.

The BioFibers creation was performed by the following sequential stages: (i) soaking core-fiber into sodium-alginate/endospore solution followed by instant soaking into calcium acetate solution, (ii) drying at temperature of 23 ± 1 °C and relative humidity (RH) of 30 ± 5% for 24 h, (iii) instant soaking the hydrogel coated core-fibers into polymer/chloroform solution (denoted as shell layer, i.e., polymer blend of polystyrene (PS) and polylactic Acid (PLA) polymer blend (1-to-1 wt.%), chloroform as the solvent, with solute-to-solvent ratio of 18 w/v, single layer coating), and (iv) drying at temperature of 23 ± 1 °C and relative humidity (RH) of 30 ± 5% for 2 h. The created BioFibers had an average diameter and density of 1.07 mm, and of 2.12 g/cm^3, respectively (Khaneghahi et al., 2023a). The endospore-laden hydrogel coating had a water-uptake capacity of 4.41 $g/g_{core\text{-}fiber}$ at 15-min exposure to distilled water (Khaneghahi et al., 2023a). The shell coating performance was evaluated via fluid ingress and abrasion resistance survivability test, detailed experimental program and the results can be found in (Khaneghahi et al., 2023a, 2023b). The results indicated the feasibility of the developed BioFibers for concrete applications (Khaneghahi et al.,

2023a, 2023b).

2.2. Sample preparation/collection

In order to enable the MICCP process in BioFibers, a precise cut using a microsurgical blade was created in the outer shell layer of BioFibers, exposing the inner hydrogel to the bio-agent solution. Subsequently, these BioFibers were exposed to the aqueous solution containing 20 g/L of yeast extract (Sigma-Aldrich, CAS:8013-01-2), and 20 g/L of urea (Alfa Aesar, CAS:57-13-6). The solution successfully penetrated through the cut surface of shell, reaching the inner endospore-laden hydrogel layer. The hydrogel then absorbed the solution and started to swell and led the endospores diffusing out to the solution (detailed information are discussed in Section 3.1, Fig. 1. As the swelling progressed in hydrogel layer, swelling pressure exerted on the outer shell led to occurrence of longitudinal fractures along the BioFibers length on the shell layer (see section 3.1). This phenomenon resulted in bonding failure between hydrogel and outer shell, exposing entire hydrogel surface to the solution and facilitating the release of endospores into the nutrient solution.

To initiate MICCP, two methods were employed to introduce a calcium source. The first method involved adding 20 g/L of calcium acetate initially along with yeast extract and urea (denoted as iCa scenario). The second method consisted of adding calcium acetate (20 g/L) in the final stage after incorporating yeast extract and urea (denoted as fCa scenario). The two methods of introducing calcium acetate were employed to explore the impact of calcium source availability on Microbially Induced Calcium Carbonate Precipitation (MICCP) kinetics. In real self-healing condition, the calcium source may be introduced into the cementitious matrix or rely on the calcium source from cement hydration products, such as calcium hydroxide. In this context, calcium availability is influenced by the diffusion rate of calcium ions leaching into the crack volume upon BioFiber activation. Through the use of these methods in our simulated MICCP, we aimed to investigate both a lower and upper bound for MICCP kinetics, providing insights relevant to practical self-healing applications. As calcium acetate was added to the system, the carbonate end-product of metabolic reactions reacted with calcium ions, precipitating calcium carbonate, as shown in Eq. (6). After MICCP termination, the BioFibers were collected from the solution, embedded in a low-viscosity epoxy resin to preserve their structure and the fractured surface for morphological analysis. The solution media was centrifuged for 9 min at 7830 rpm and a temperature of 25 °C to terminate the MICCP process, and separating the yeast extract, urea, and calcium solution from the precipitated solid residue (the precipitation collection shown in Fig. 2). Then, the sedimented residue was collected and heated at 105 °C for 1 h to remove the remaining moisture from the samples, resulting in solid pellets in the container. Then, the solid pellets were finally ground to collect the particles with a size of less than 75 μm for characterization experiments. The.

2.3. Experiments

2.3.1. Thermogravimetric analysis

To determine the calcium carbonate precipitation kinetics, thermogravimetric analysis (TGA) was performed on the precipitated solid residue collected from BioFibers at different MICCP time intervals. TA Instrument Q5000-IR was used for TGA experiment on 20–30 mg of powder residue at temperature ranging from 30 to 900 °C with an increment rate of 10 °C/min under inert nitrogen gas with a flow rate of 10 ml/min. To quantify the calcium carbonate content in the precipitations, the weight loss at 600–800 °C is associated to the CO_2 releasing the system due to the decomposition of calcium carbonate ($CaCO_3$) to calcium oxide (CaO) and CO_2 (Scrivener et al., 2016). Based on the weight loss reported at this temperature range, the quantity of calcium carbonate in the sample can be calculated based on the following equations:

$$W_{CaCO_3} = W_{CO_2} \times \left(M_{CaCO_3} / M_{CO_2}\right) \quad \text{Eq. 7}$$

$$W_{CaCO_3/g_{Solid}} = W_{CaCO_3} / \left(W_i - W_{H_2O}\right) \quad \text{Eq. 8}$$

$$W_{CaCO_3,t} = W_{CaCO_3/g_{Solid}} \times W_{Residue} \quad \text{Eq. 9}$$

In Eq. (7), W_{CaCO3} is the weight percentage of $CaCO_3$ presents in the tested sample, W_{CO2} is the weight loss measured in the temperature range of 600–800 °C, and M_{CaCO3} and M_{CO2} are the molar weight of $CaCO_3$ and CO_2 with the values of 100.09 g/mol and 44.01 g/mol, respectively. To remove the effect of moisture absorbed during TGA sample preparation, the $CaCO_3$ weight percentage is normalized to the total weight of solid (W_{CaCO3}/g_{Solid}) using Eq. (8). In this equation, W_i is the total weight of tested samples before heating, and W_{H2O} is the weight loss measured at 30–105 °C. The values of W_{CaCO3}/g_{Solid} shown the quantified amount of $CaCO_3$ in percentage, not the total weight of precipitated calcium carbonate per BioFiber, denoted as $W_{CaCO3,t}$. To calculate this value using Eq. (9), the percentage values obtained in Eq. (8) are multiplied by the total weight of collected residue from each BioFiber.

2.3.2. Scanning electron microscopy and energy-dispersive spectroscopy

Zeiss Supra 50VP field-emission scanning electron microscopy (SEM) using secondary electrons was performed to determine morphology, surface features and textures on BioFiber prior/post MICCP activation. Due to nonconductivity of BioFiber elements, the samples were coated with 9–12 nm 80/20 platinum/palladium using Cressington 208 sputter coater prior to scanning. SEM was equipped with Energy-Dispersive X-ray Spectroscopy (EDS) high silicon drift detectors (SDD) for surface elemental analysis on the powder precipitated residue. EDS revealed further insights into elemental composition of the precipitated solids at different stage of MICCP process. For sample preparation, the 2 g of solid pellets were collected from BioFiber precipitation, dried at 105 °C for 1 h, then grinded to obtain the particle size of <75 μm.

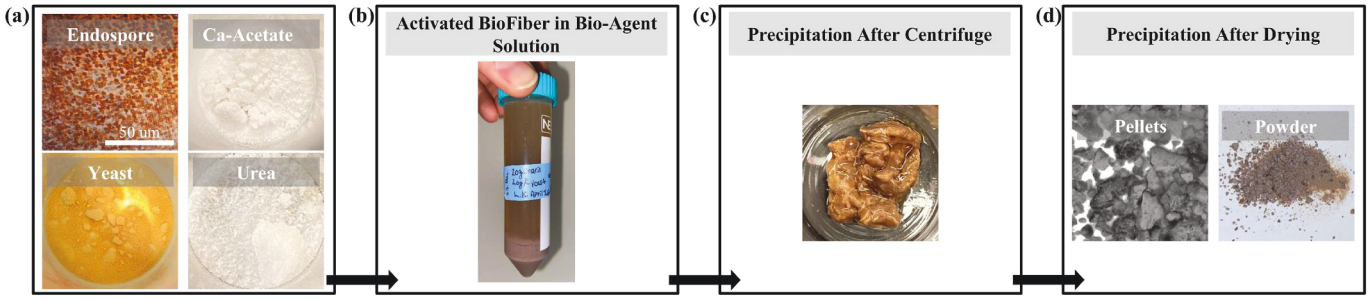

Fig. 2. (a) Bio-agent components, (b) activated BioFiber in bio-agent solutions after MICCP, (c) collected precipitation from solution via centrifuge, and (d) collected solid particles after drying stage, in form of pellets and powder.

2.3.3. X-ray diffraction

X-ray diffraction (XRD) was carried out on powder residue to characterize the crystal structural properties of BioFiber precipitations using qualitative and quantitative phase analysis. For qualitative phase identification, calcium carbonate polymorph phases were identified from the XRD graph. For quantitative phase analysis, the precipitated powders were blended with 10 wt% TiO_2 Rutile (99% reagent grade), as an external reference material) having 100% crystalline phases. Through this approach, the crystalline/amorphous phases were quantified in each sample. Benchtop X-ray diffractometer Rigaku-MiniFlex 600 equipped with Cu Kα (λ = 1.387 Å) was used at Bragg angle 2θ in the range of 20°–80° with a step of 0.02°.

The XRD data were then analyzed using a Rietveld refinement open-source software named Profex (Doebelin and Kleeberg, 2015). In the case of a multi-phase XRD pattern, the datasets of the substances are normalized to a fully crystalline reference sample (Döbelin, 2020; Hill, 1991). The correlation between the absolute phase quantity and the intensity of a phase's signal contribution is directly proportional to the Rietveld scale factor (*S*) (Hill, 1991). The scale factor for phase A (S_A) in any sample of known composition was calculated as follows:

$$S_A = \frac{W_A \bullet K}{(Z.M.V)_X \bullet \mu_m^*} \quad \text{Eq. 10}$$

where K is an instrument dependent scaling factor, Z is the number of formula units per unit cell, M is the mass of the formula unit, V is the unit cell volume, and μ_m* is the bulk mass absorption coefficient of the specimen (Dinnebier and Billinge, 2008). W_A is the absolute weight fraction of phase A. In the case of phase-pure reference pattern, the scale factor S_r is (Döbelin, 2020):

$$S_r = \frac{1 \bullet K}{(Z.M.V)_X \bullet \mu_r^*} \quad \text{Eq. 11}$$

In order to scale the intensity of reference pattern (I_r) to a weight fraction in a multi-phase sample, it must be multiplied with the relative scale factor as (Döbelin, 2020; Hassan and Anwar, 2010):

$$I_X = I_r \bullet \frac{S_X}{S_r} = I_r \bullet \frac{W_X}{\left(\frac{\mu_m^*}{\mu_r^*}\right)} \quad \text{Eq. 12}$$

where μ_r* is the mass absorption coefficient of the reference material, and μ_m* is calculated as:

$$\mu_m^* = \frac{\sum_{i=1}^{n}\left(\mu_i^* \bullet W_i\right)}{n} \quad \text{Eq. 13}$$

where μ_r* and W_i are the mass absorption coefficient and phase quantity of phase i. The simulated diffraction pattern is obtained by summing all the rescaled intensities of phases *i* to *n*:

$$I_{sum} = I_A + I_B + \cdots + I_n \quad \text{Eq. 14}$$

By applying a synthetic noise patter for intensity I_{sum}:

$$I_{sim} = I_{sum} + p\left(\sqrt{I_{sum}}\right) \quad \text{Eq. 15}$$

where *p(x)* function generates a random Posson-distributed number for x counts. The phase composition of the diffraction pattern I_{sim} is known from the W values selected for each phase. As blended with 10 wt% TiO_2 Rutile (reference materials) to precipitation specimens, the weight fraction of rutile is known, and through Rietveld refinement, the weight fraction for calcium carbonate polymorphs (calcite, vaterite, and aragonite) and amorphous content were quantified.

3. Results and discussions

3.1. Morphology and microstructural analysis

This section aimed to study and compare the morphological characteristics of the developed BioFiber before and after the activation process. The term "BioFiber activation" refers to the exposure of fractured BioFibers to a healing reagent solution containing a carbon/urea/calcium source (the details regarding the solutions are given in section 2.2). Fig. 3(a–c) shows optical microscopic images of the BioFibers elements as core-fiber, core-fiber with endospore-laden hydrogel coating, and core-fiber with endospore-laden hydrogel coating with outer shell layer. These images indicated the uniform surface on the core-fiber in both hydrogel and shell coatings. The uniformity in the hydrogel/shell surface functionalization on the core-fiber allowed control over functionalities of hydrogel and shell layer, including controlled swelling and endospore delivery for hydrogel, while ensuring impermeability for shell. Furthermore, uniformity in BioFiber production allowed consistency in the resulting properties, specifically MICCP activity which is the primary objective of this study. The comprehensive results regarding the physical properties, e.g., diameter and hydrogel/shell thickness, of the BioFibers made with different material options have been reported in our previous paper (Khaneghahi et al., 2023a, 2023c). In Fig. 3 (d), a fractured BioFiber before MICCP activation is shown. This image demonstrated the swollen hydrogel after exposure to solution and the longitudinal cracks in the outer shell due to swelling pressure. This phenomenon in BioFiber benefits the MICCP activity by exposing a larger surface area of the hydrogel to solution and promoting endospores distribution from hydrogel to the surrounding environment where self-healing end-product is needed.

To have a deeper understanding of BioFiber microstructures after MICCP, SEM images were obtained in the fractured/swollen stage of BioFiber, prior to MICCP activation, as shown in Fig. 4. This figure highlights the presence of swollen hydrogel layer and fractured outer shell on the core-fiber. It is important to note that the SEM images shown in this figure were captured after the drying swollen BioFiber under ambient condition; hence, the hydrogel shown here is in deswelling/drying phase following one cycle of swelling. Upon closer inspection of the shell surface, these SEM images revealed the longitudinal fractured surface developed on one side of the shell layer as a result of the swollen hydrogel, while the other sides of the shell remained intact. This observation suggests that the BioFiber activation predominantly originated from one side, rather than inducing cracks in all directions across the shell surface.

As the BioFibers activated upon exposure to healing reagent, MICCP occurred, and sacrificial samples were collected at ½, 1, 2, 3, 4, 5, 6, 10, 14, 21, and 28 days of MICCP process. Fig. 5 displays the optical microscopic images of the activated BioFibers with fractured shell layer and adhered solid precipitations to the core-fiber and inner/outer area of the shell. These images revealed that the amount of dark solid residue built up on the BioFibers increased as the chemical/biological reactions progressed over time. The solid residues observed in these images were postulated to be the combination of precipitated calcium carbonate and remaining organic matter. From the observation of SEM images of BioFiber after 10-day MICCP (as depicted in Fig. 6), it is evident that a significant quantity of precipitations accumulated on both core-fiber and shell. The precipitations exhibited sizes ranging from less than 1 μm–30 μm. The different range of particle sizes indicated distinctive and heterogenous distribution of the solid residues, which can be attributed to various calcium carbonate polymorphs. Fig. 7 displays dead vegetative cells observed in the precipitates obtained after 10 days. These SEM images reveal that the endospores delivered via BioFibers underwent germination, transformed into vegetative cells, and were detectable in SEM images following the termination of MICCP. Additionally, the size of the vegetative cells was observed within the range of 1–3 μm. Noted that the optical microscopic and SEM images discussed earlier

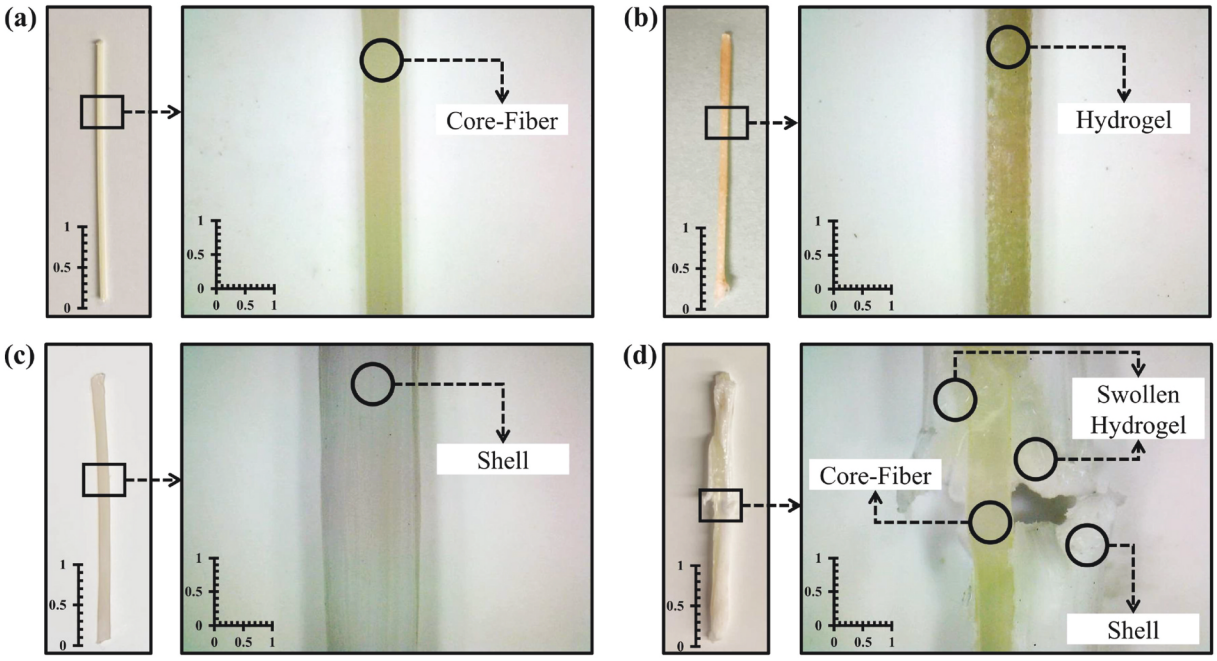

Fig. 3. PVA core-fiber, (b) endospore-laden hydrogel core-fiber, (c) BioFiber with outer PS:PLA shell coating, (d) BioFiber post-fracture/swelling prior-MICCP.

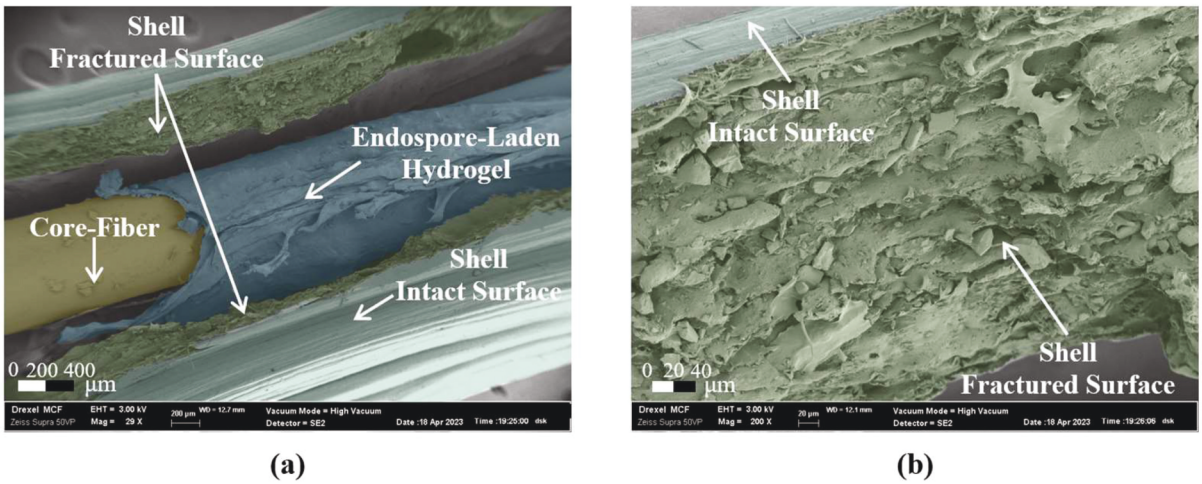

Fig. 4. SEM images at post-fracture/swelling prior-MICCP stage of (a) BioFiber, (b) outer shell. (Note that the SEM images were colorized to have a better representation of the components).

specifically depicted the BioFibers, not the precipitates obtained through solution centrifugation. To gain a better understanding of the kinetics and the morphological characteristics of self-healing end-product, the following sections will focus on analyzing the precipitates in the form of pellets and solid particles.

3.2. Precipitation kinetics analysis

TGA experiments were performed on the precipitated particles with the procedure described in section 2.3.2. Figs. 8 and 9 show the thermogravimetric results in the form of weight loss and derivative values against temperature for fCa and iCa scenarios, respectively. As evident in this figure, three major weight losses were observed in all the samples at temperature ranges of ~: (i) 30–105 °C, (ii) 200–600 °C, and (iii) 600–800 °C. The weight loss at temperature below 105 °C was attributed to the loss of physically bound water in the solid particles, indicating the remaining moisture content in the samples. The second weight loss, initiating at 200 °C continued up to temperature of 600 °C, corresponds to the decomposition of organic matter (Ferral-Pérez et al., 2020; Nielsen et al., 2020; Rodriguez-Navarro et al., 2007).

The calculated values of W_{CaCO3}/g_{Solid} and $W_{CaCO3,t}$ for each sample at different MICCP intervals are shown in Fig. 10, indicating the calcium carbonate precipitation kinetics. This figure revealed a plateau behavior in precipitation kinetics for samples exposed to healing reagent solutions for up to 3 days for fCa scenario and 5 days for iCa scenario. This phenomenon in fCa scenario can be attributed to the lag phase in endospore germination, i.e., the physiological changes required for endospores to enter the vegetative growth stage, and temporary inhibition of urea for bacterial growth and urea hydrolysis phase (Rahmaninezhad et al., 2022a, 2022b). During this lag phase, ureolytic activity can be limited, resulting in lower production of carbonate ion (CO_3^{2-}) concentration needed to react with Ca^{2+}. For scenario iCa, the lag phase continued for additional two days. Our hypothesis suggests that the inhibition may arise from a combination of factors, including (i) a change in the initial

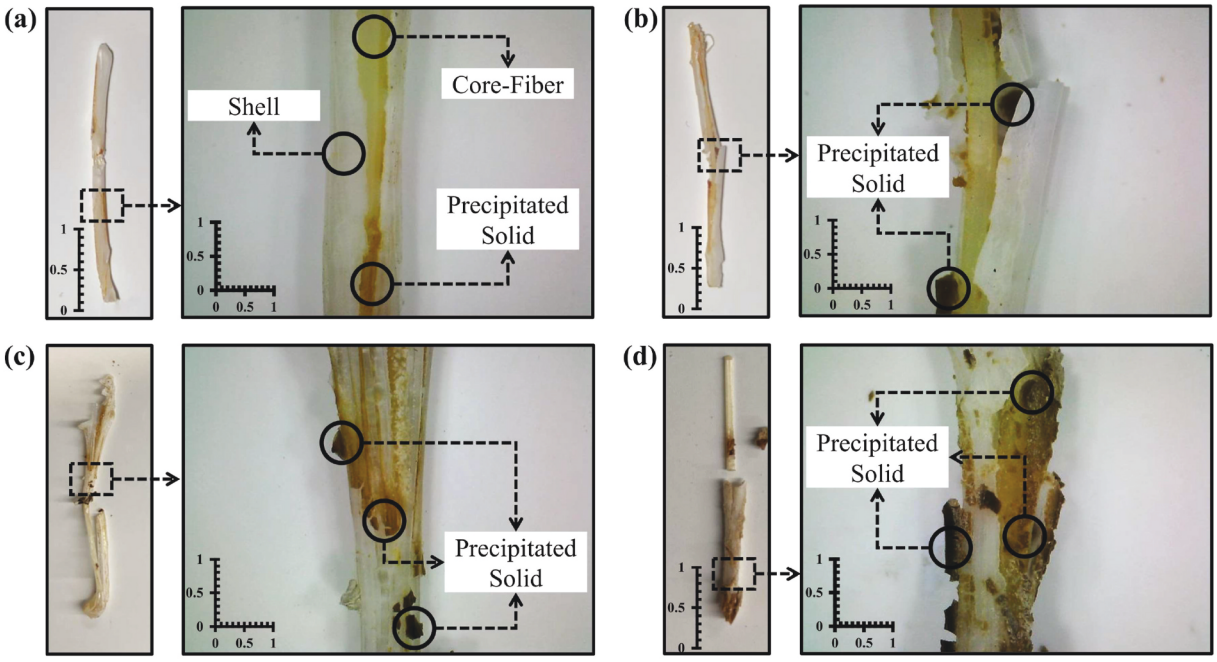

Fig. 5. BioFiber after MICCP activation (fCa scenario) at different time interval (a) ½ day, (b) 3 days, (c) 6 days, (d) 10 days.

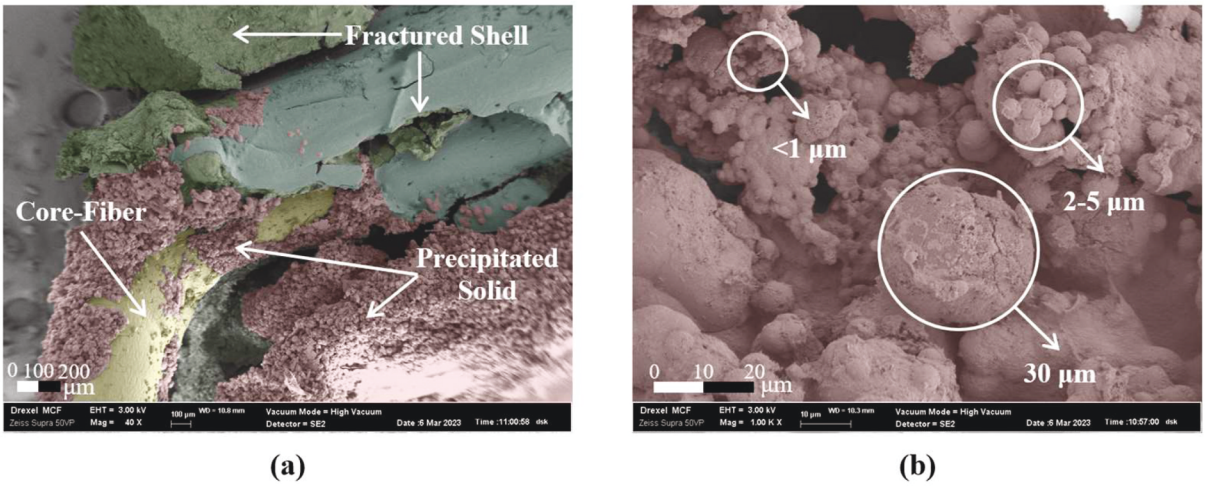

Fig. 6. SEM images at post-MICCP stage (fCa scenario, 10-day) of (a) BioFiber, (b) precipitation solid adhered to BioFiber. (Note that the SEM images were colorized to have a better representation of the components).

pH due to the addition of calcium acetate, (ii) the formation of biofilms on calcium carbonate precipitation leading to a reduction in the initial concentration of vegetative cells, and (iii) inhibition in urease release due to a lower germination phase and outgrowth. However, on the fourth day for fCa and sixth day for iCa scenario, an increase was observed in the amount of calcium carbonate precipitation, higher increase rate in fCa. This can be associated with the revival of ureolytic activity due to an increase in urease release by germinated vegetative cells. After this sudden increase, a gradual increase in the amount of calcium carbonate until day 6. Furthermore, the samples exposed for more than 10 days in fCa and 14 days in iCa scenario, another significant increase in quantity of calcium carbonate was observed, which can be attributed to an increase in saturation degree of CO_3^{2-}. As shown in Fig. 10 (b), the weight of calcium carbonate precipitation in fCa scenario showed an increase from 3.35 mg per BioFiber after ½ day to 139.41 mg within 6 days, reaching 397.55 mg in 10 days, eventually achieving 620.08 mg in 28 days. For iCa scenario, the calcium carbonate content calculated to be 5.47, 133.75, and 583.31 mg for ½, 10, and 28 days MICCP, respectively. The comparison between fCa and iCa scenarios indicated that after 21 days MICCP, the calcium carbonate precipitation content (both percentage and residual weight) in both scenarios converged after 21 days. The results indicated that after 21 days, the calcium carbonate precipitation reached the maximum upon consumption of all urea and yeast extract in the system.

The weight calculations can be employed to estimate the precipitation volumes, which serve as an indicator of the crack volume healing efficiency for each activated BioFiber. However, calculating the exact volume of precipitated calcium carbonate was not applicable at that point because the density of calcium carbonate varies depending on whether it is in the amorphous or crystalline phase, as well as differing among various polymorphs (Kitamura, 2001). TGA results revealed the precipitation kinetics for activated BioFibers which can be denoted as the reactions kinetics for self-healing process. The self-healing kinetics indicated that the biological/chemical processes exhibited three phases

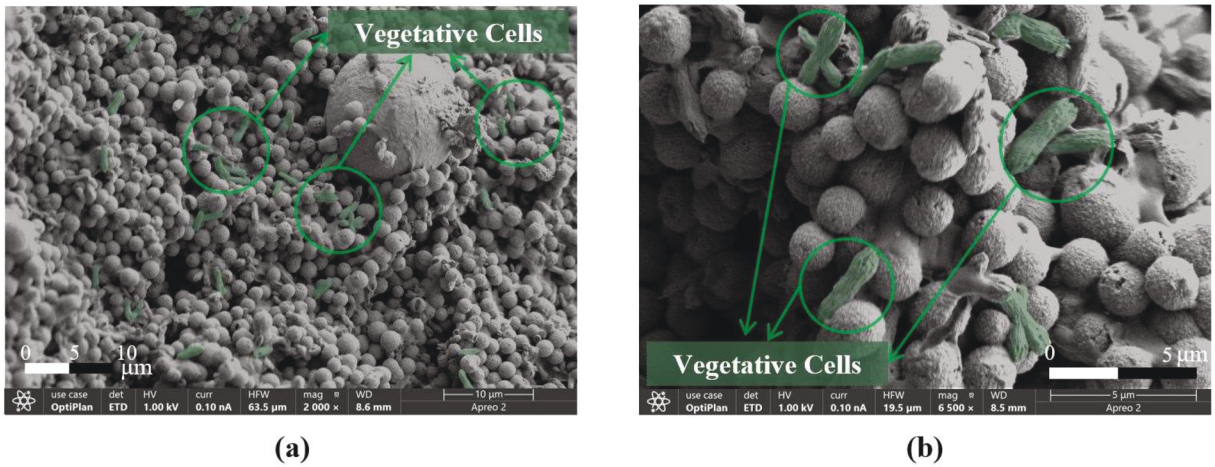

Fig. 7. SEM images at post-MICCP stage (fCa scenario, 10-day) indicating dead vegetative cells (colored as green) in precipitations, (a) magnification: 2kX, (b) magnification: 6.5kX. (For interpretation of the references to color in this figure legend, the reader is referred to the Web version of this article.)

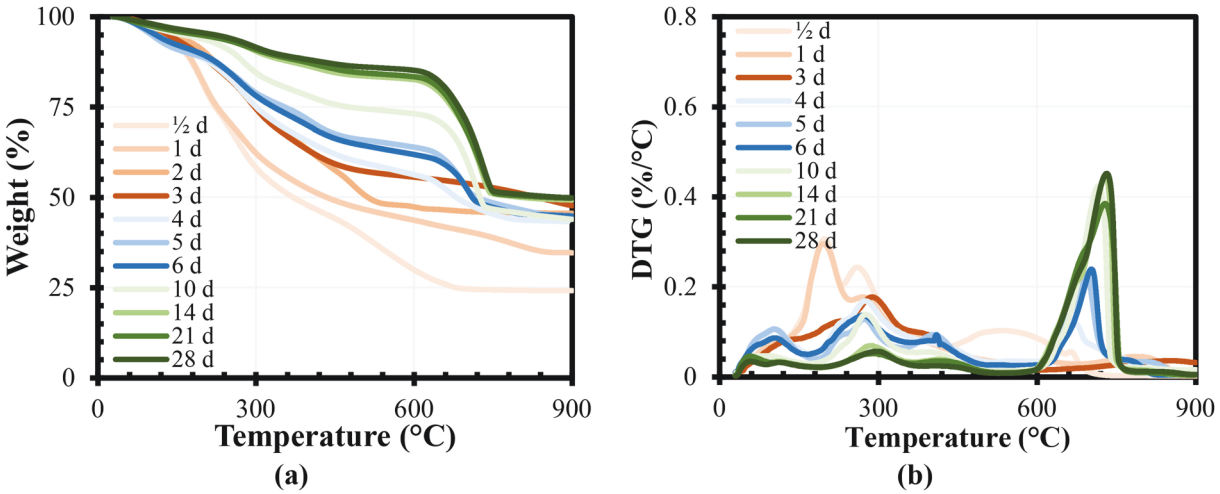

Fig. 8. Thermogravimetric analysis results on BioFiber precipitation for fCa scenario: (a) weight loss (%), (b) weight loss derivative with respect to temperature denoted as DTG (%/°C).

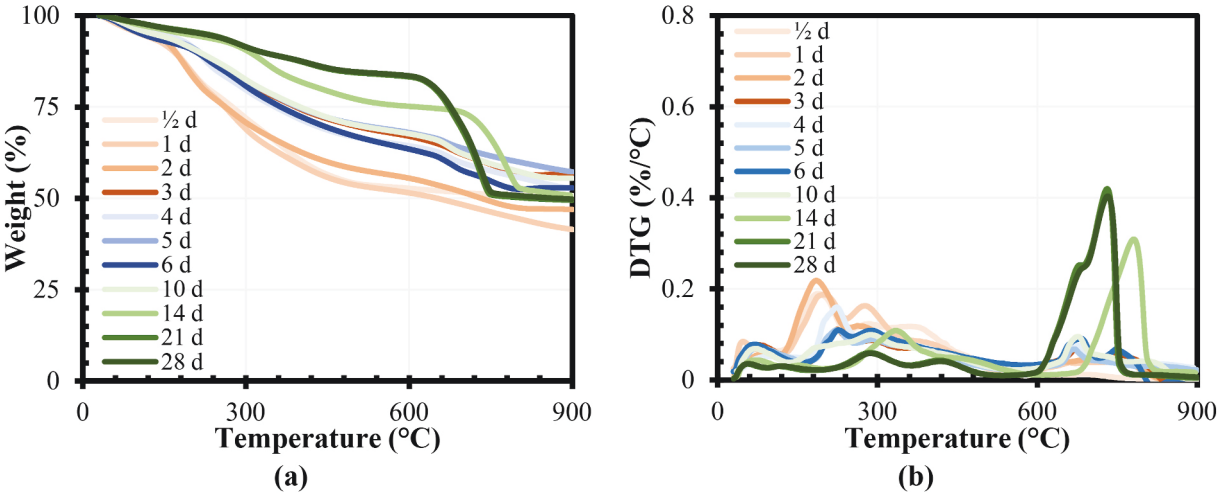

Fig. 9. Thermogravimetric analysis results on BioFiber precipitation for iCa scenario: (a) weight loss (%), (b) weight loss derivative with respect to temperature denoted as DTG (%/°C).

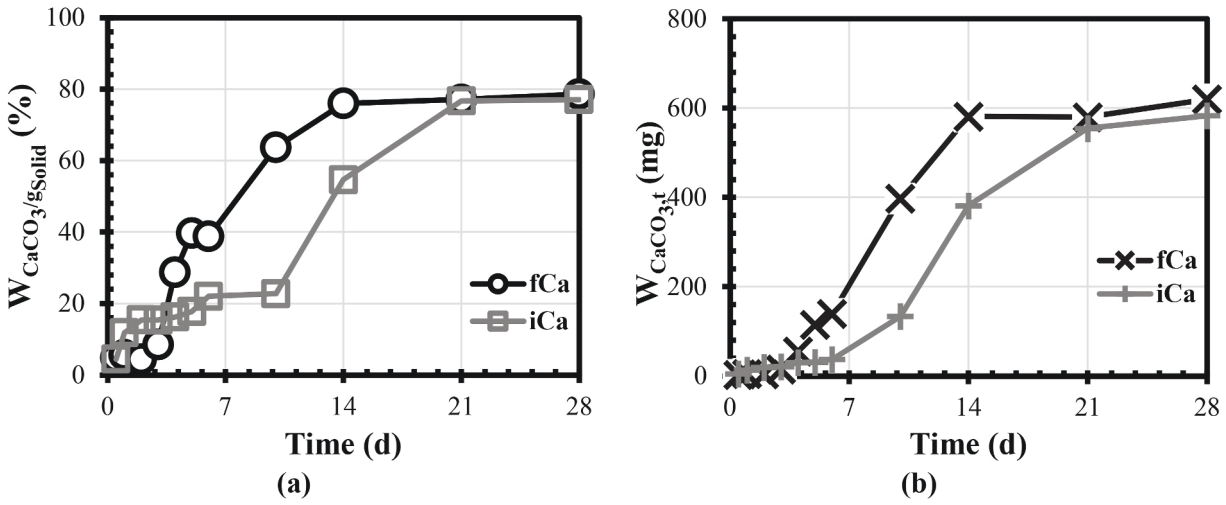

Fig. 10. Amount of calcium carbonate precipitated over time (a) weight percentage normalized to weight of solid residue, (b) calcium carbonate weight per activated BioFibers.

as: (i) the availability of germinated cells as nucleation site (fCa: T ≤ 3 d, iCa: T ≤ 5 d), (ii) the urease-catalyzed reactions (fCa: 3 d < T ≤ 6 d, iCa: 6 d < T ≤ 10 d), and (iii) the saturation degree of carbonate (fCa: 10 d ≤ T, iCa: 14 d ≤ T). In real-world conditions, we postulate that the actual kinetics of self-healing in practical applications adhere to a three-stage trend, falling within the range of precipitation kinetics observed for scenarios involving finally added calcium (fCa) and initially added calcium (iCa). To have a deeper understanding of the self-healing morphology and crystal structure on precipitation, the results presented and discussed in the following sections focused on the precipitations acquired during the three-stage time interval for scenario fCa.

3.3. Elemental analysis

To probe the elemental composition changes of the precipitations on the micro-scale, EDS were performed on the samples collected on the time interval of T ≤ 3 d, 3 d < T ≤ 6 d, and 10 d ≤ T for fCa scenario, from now on denoted as *S*–I, *S*-II, and *S*-III. SEM equipped with EDS was performed in regions-of-interest with the area of 600 × 750 μm. Fig. 11 displays the elemental composition mapping and EDS spectroscopy showing the elements relative abundance on the samples. In the samples collected at T ≤ 3 d, the trace for phosphorus, potassium, nitrogen, sodium, and sulfur were captured in EDS spectroscopy. In the thermal shock endosporulation methods, the vegetative cells were treated with incubated into Minimal Salt Media (MSM) (Rahmaninezhad et al., 2022b), may result in endospore storing nutrients such as carbon, phosphate, and nitrogen in the form of granules. Upon germination, storage granules in the inner endospore membrane were believed to release phosphorus, sodium, and potassium into the media (Tocheva et al., 2013). Therefore, the presence of elements such as nitrogen and phosphorus along with carbon and oxygen can be an indication of higher organic matter content in the samples. In addition, the trace of phosphorus, potassium, sodium, and sulfur in this phase may be attributed to the remaining yeast extract in the dead cells (Chan-u-tit, Laopaiboon, Jaisil and Laopaiboon, 2013). In the second stage, i.e., 3 d < T ≤ 6 d, EDS results indicated the increase in the presence of oxygen, calcium, and carbon which was related to the higher precipitation of calcium carbonate. Moreover, there was a higher trace of phosphorous in the results, acknowledging progress in the cell outgrowth phase led to the release of these elements from bacterial storage granules. In the third stage, i.e., 10 d ≤ T, the primary elements found in the samples were calcium, oxygen, and carbon, indicating higher calcium carbonate which was aligned with TGA results.

3.4. Crystal structure analysis

To determine the crystal structure of the precipitations obtained from BioFibers, a series of characterization techniques, including qualitative/quantitative XRD, SEM, and TGA, were conducted on the powder collected from *S*–I, *S*-II, *S*-III. Initial work was completed using qualitative XRD and SEM imaging to identify and analyze the calcium carbonate polymorphs precipitated via MICCP. The qualitative XRD results, as shown in Fig. 12 (a), revealed that the dominant calcium carbonate crystalline form in *S*–I was vaterite, while transforming to the vaterite and calcite in *S*-II and *S*-III. In general, the MICCP-driven calcium carbonate crystallization is a multistep transformation process as: (i) initiation with amorphous calcium carbonate (ACC) precipitations, (ii) undergoing crystallization phase via ACC-to-vaterite transformation, and (iii) transformation from metastable vaterite to calcite via dissolution-reprecipitation stages (Chekroun et al., 2004; Pichon et al., 2008; Pouget et al., 2009; Van Paassen, 2009). By looking at the SEM images shown Fig. 12 (b), it was observed that the precipitations in *S*–I (pH of ~7.3–7.7) were mainly composed of amorphous content, indicating randomly distributed and loosely packed particles. The amorphous content in this stage was speculated to be ACC and the remaining organic matter in the residue. In *S*-II (pH of ~8.1–8.9), spherical particles with median size of 1–3 μm were observed which were believed to be vaterite crystals (Song et al., 2020). This observation acknowledged the ACC-to-vaterite transition due to increase in thermodynamic stability from *S*–I to *S*-II. Finally, in *S*-III (pH of ~9.2–9.5), spherical particles size continued to increase even up to 10–20 μm, which can be attributed to irregular calcite and/or agglomerated vaterite particles formed due to Oswald maturation (Oral and Ercan, 2018; Song et al., 2020). It was postulated that the majority of ACC have been consumed in *S*-III, favoring continuous vaterite nucleation and spherulitic growth in particles from *S*-II to *S*-III (Bots et al., 2012).

To better understand the calcium carbonate precipitation and crystallization process, we conducted quantitative XRD along with TGA to determine the amorphous and crystalline content in the samples. Based on quantitative phase analysis, the weight fraction of each calcium carbonate polymorphs and the total amorphous content were calculated in the samples. However, as discussed earlier, the amorphous content was assumed to be the mixture of organic content and ACC. To distinguish these amorphous contents, TGA was performed to quantify the total organic content in the samples (see Fig. 13). By using TGA results, the organic content in the samples was defined as the total fraction weight of the samples subtracted by the amount of moisture and calcium carbonate in the system. The amount of ACC in the system was then

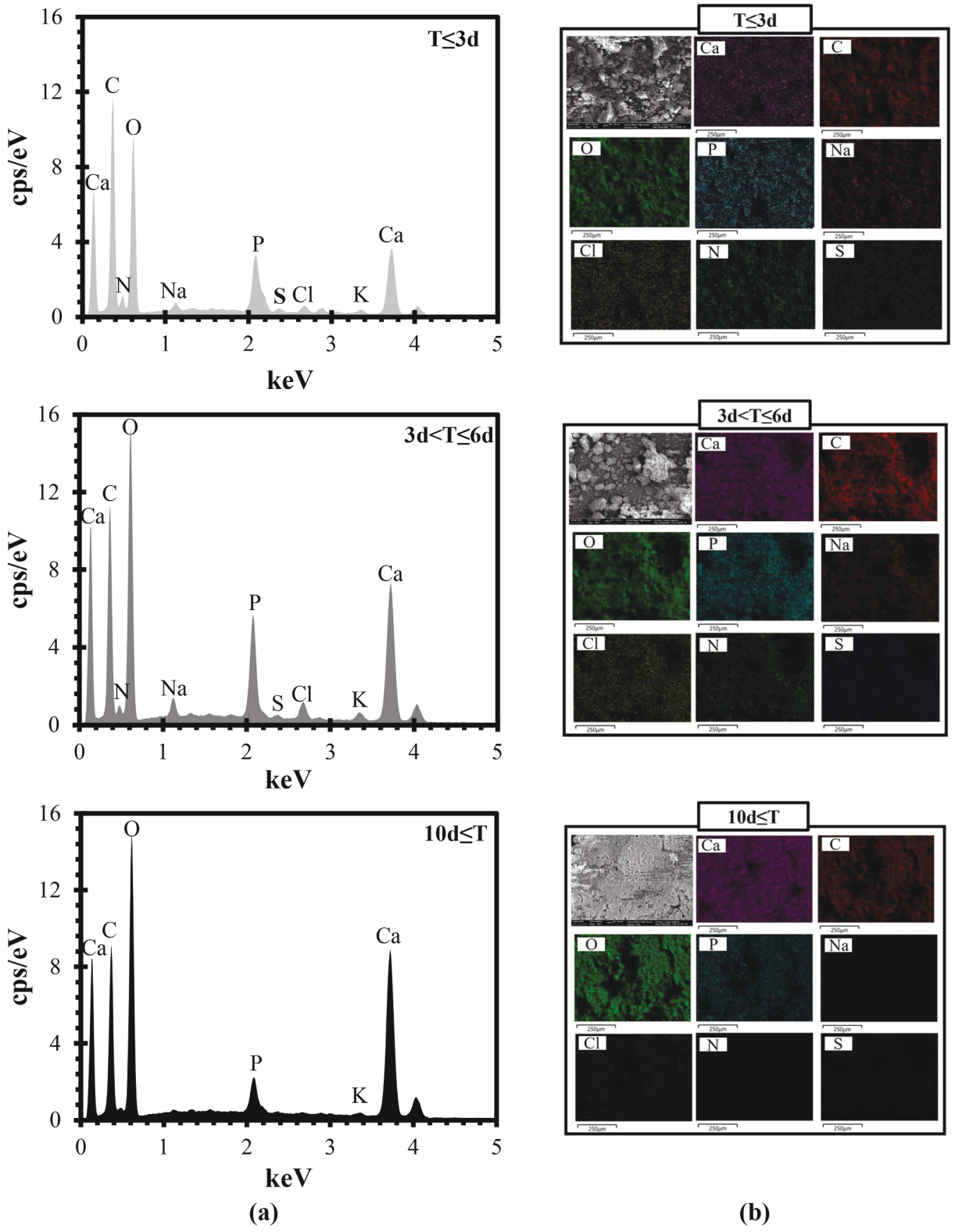

Fig. 11. Elemental analysis on the precipitated solid residue: (a) EDS spectrum, and (b) EDS elemental mapping.

calculated based on the difference between total amorphous content, determined via quantitative XRD, and organic content, obtained by TGA.

The quantitative results indicating weight fraction of calcite, vaterite, aragonite, ACC, and organic matter are shown in Fig. 14. The results stated that the amorphous phase detected previously was mainly organic matter, with slight ACC portion in all the stages. This observation revealed that ACC-to-vaterite transformation was a rapid process, leaving small quantity of ACC in the collected samples, i.e., 5.6, 8.6, and 2.5 wt% in *S*–I, *S*-II, and *S*-III, respectively. In terms of organic matter, the quantity decreased as MICCP progressed, acknowledging the increase in precipitated calcium carbonate relative to organic matter,

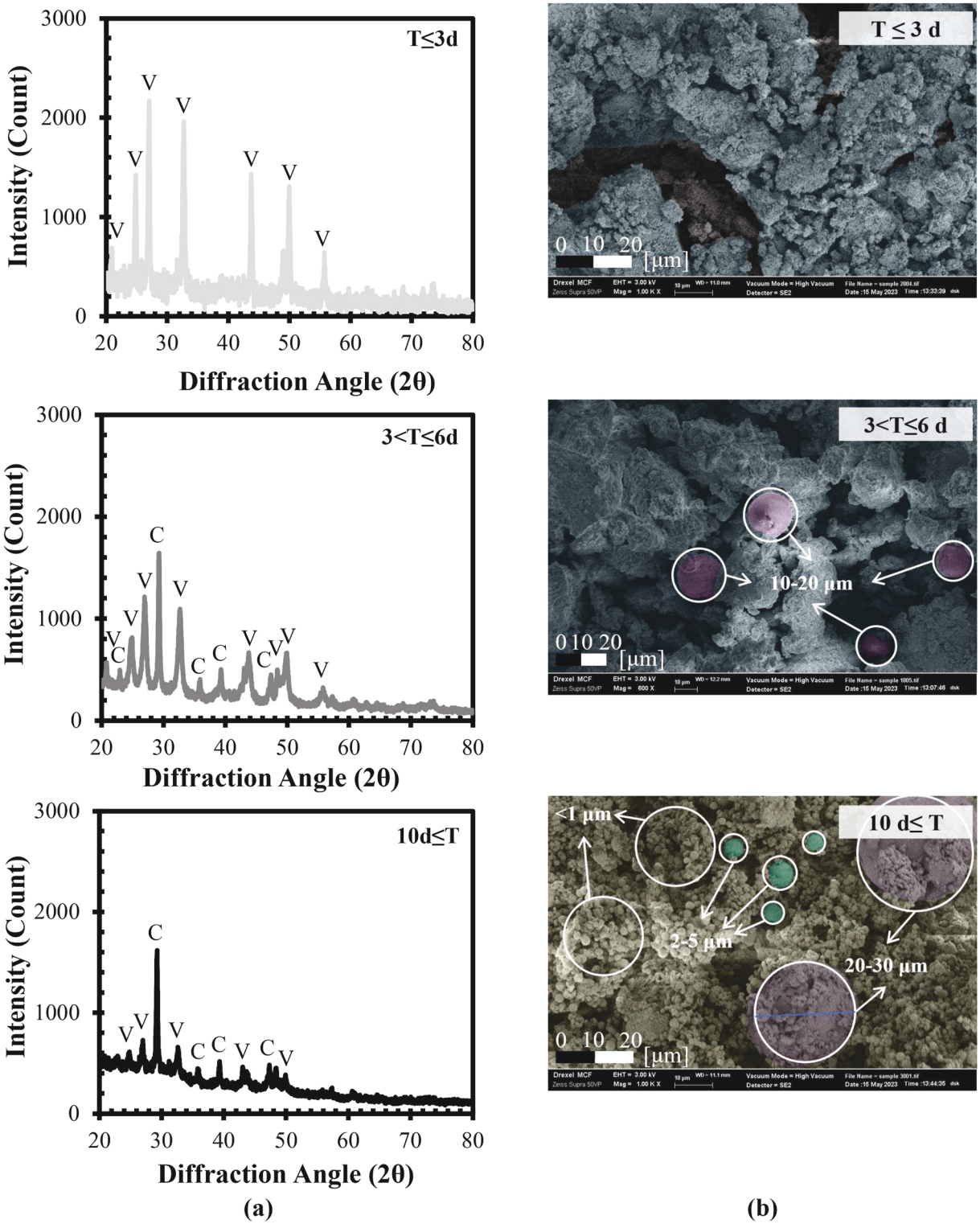

Fig. 12. (a) Qualitative phase detection XRD results, (b) SEM Results of precipitated solids.

which was also proved by self-healing kinetics data (shown in Fig. 10). When it comes to calcium carbonate polymorphs, the main portion of precipitated calcium carbonate in all the stages was vaterite crystals, with 55.86, 65.14, and 67.67 wt% of calcium carbonate to be vaterite in *S*–I, *S*-II, and *S*-III, respectively. The quantitative phase analysis results also correlated with SEM images (shown in Fig. 12) displaying vaterite crystals in the samples. One of the reasons that mainly vaterite phase formation was stabilized in the system can be due to the presence of extracellular polymeric substances (EPS) in bacterial surface interacting with the environment. It has been studied that EPS had significant impact on stabilizing thermodynamically unstable vaterite, particularly in basic pH conditions which was the case in our study having a pH of 9–10 in the system (Hammes et al., 2003; Szcześ et al., 2016; Wen et al., 2020; W. Zhang et al., 2018). In addition, vaterite being the dominant phase as MICCP products can be attributed to the calcium source in this study, which was calcium acetate. Previous studies showed that by

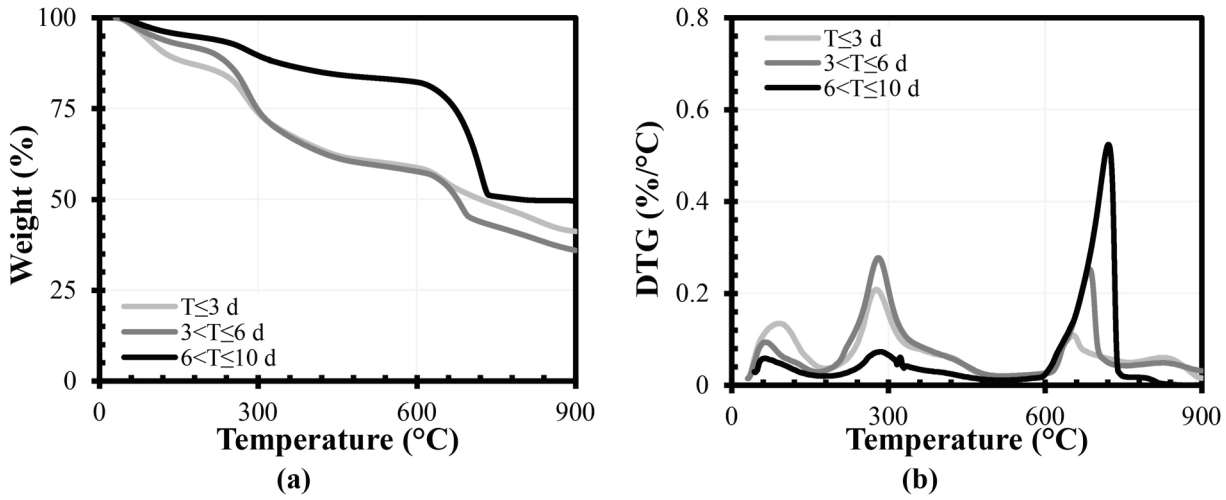

Fig. 13. Thermogravimetric analysis on the precipitated solids coupled with XRD quantitative analysis (a) TGA, (b) DTG.

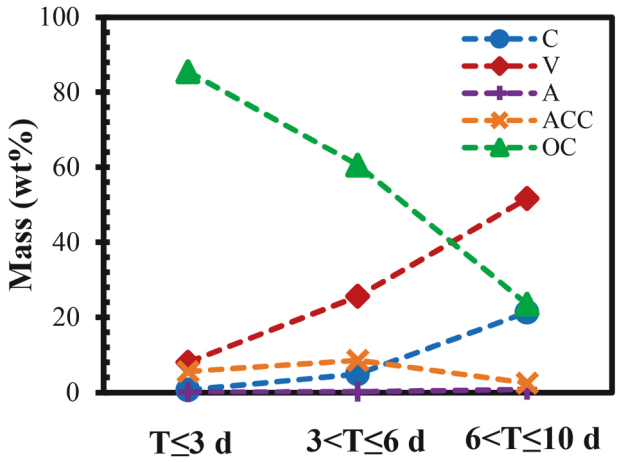

Fig. 14. Quantitative analysis on precipitated solids indicating the mass ratio of calcite (C), vaterite (V), aragonite (A), amorphous calcium carbonate (ACC), and organic content (OC).

changing the calcium source from calcium acetate to calcium nitrate or calcium chloride, the main product shifted from vaterite to calcite (Lv et al., 2023). Furthermore, quantitative phase analysis revealed that higher content of calcite was observed as MICCP progressed over time, from 4.83 wt% in *S*–I to 12.46 wt% in *S*-II, and 28.01 wt% in *S*-III. Moreover, the quantitative/qualitative XRD results stated that almost no aragonite was observed in the system.

4. Summary and conclusion

This study evaluated the biomineralization performance of the multi-purpose endospore-laden polymeric fibers (BioFibers) used for self-healing applications in quasi-brittle composites. The end-product delivered by activated BioFibers was calcium carbonate providing self-healing capability into various materials such as cementitious composites. In the current study, the BioFiber self-healing was conducted within a controlled laboratory environment, i.e., solution, to obtain the preliminary insights for the BioFiber self-healing performance in cementitious matrix. It is essential to acknowledge the controlled nature of the setting, recognizing that the results may differ in a real-world self-healing condition. This preliminary investigation serves as a foundation for the future research, providing valuable observations while emphasizing the distinction between controlled self-healing conditions in the solution and cementitious matrix. To assess biomineralization performance, various analyses were conducted on self-healing kinetics, microstructural, elemental, and crystal structure on the precipitated materials at different time frame. This study yields several key conclusions that can be inferred as.

- The precipitation kinetics were influenced by three key factors in both iCa and fCa scenarios: (i) the presence of germinated endospore in the system (fCa: T $\leq$ 3 d, iCa: T $\leq$ 5 d, noted as *S*–I), (ii) urease content (fCa: 3 d < T $\leq$ 6 d, iCa: 6 d < T $\leq$ 10 d, denoted as *S*-II), and (iii) carbonate content (fCa: 10 d $\leq$ T, iCa: 14 d $\leq$ T, denoted as *S*-III). The calcium carbonate precipitation was limited in the first stage due to the lower number of germinated endospore due to the germination lag phase. In the second stage, a jump in the calcium carbonate content was observed which was attributed to the increase in urease-catalyzed reaction activity. In the final stage, the increase in germinated endospore and ureolytic activity resulted in higher concentration of carbonate in the system, leading to a significant increase in calcium carbonate precipitations. TGA results for fCa scenario indicated that the average weight fractions of calcium carbonate relative to weight of solid precipitations were 5.82, 35.72, and 73.84 % in *S*–I, *S*-II, and *S*-III, respectively. For iCa scenario, the average calcium carbonate contents calculated as 12.64, 22.35, and 69.47 % % in *S*–I, *S*-II, and *S*-III, respectively. In terms of the weight of calcium carbonate precipitated per BioFiber (with an average weight of 56.9 $\pm$ 1.4 mg), the average values for fCa were calculated as 7.25, 103.24, 544.66 mg was calculated for *S*–I, *S*-II, and *S*-III, respectively. When it came to iCa scenario, the average calcium carbonate weight per BioFibers changed to 18.12, 85.45, and 506.45 mg for *S*–I, *S*-II, and *S*-III, respectively.
- Elemental analysis showed abundant carbon, calcium, and oxygen in all the stages, indicating the presence of organic matter and/or calcium carbonate. However, the presence of the elements, i.e., phosphorus, potassium, nitrogen, sulfur, and sodium, mainly in the first stage, revealed that the trace of such elements were associated with the storage granules releasing these elements during germination and outgrowth phases. As MICP progressed, the trace of calcium, oxygen, and carbon in the same area indicated an increase in calcium carbonate content.
- Through qualitative/quantitative XRD and SEM, we noticed that the primary calcium carbonate formed by BioFiber was vaterite in all the stages, which partially recrystallized as calcite in the final stage (S-III). The stabilization of vaterite in the system was believed to be due to synergic effect of: (i) the basic condition of the precipitation environment (pH of ~8–9.5), (ii) use of calcium acetate, and (iii) the

presence of extracellular polymeric substances (EPS) in bacterial surface interacting with the environment.

The findings of this study stated the considerable potential of these BioFibers to produce crystalline calcium carbonate as a self-healing end-product. The results indicated that the formation of calcium carbonate polymorphs are influenced by reaction kinetics and environmental factors, such as pH and bacterial species. The results of self-healing kinetics can be further employed for predictive model development for numerical analysis. The next step of the current research is to focus on the crack growth control and self-activation functionalities through the incorporation of BioFibers in quasi-brittle matrix, mainly cementitious composites. In addition, our future studies will involve evaluation of BioFiber/matrix interfacial properties, BioFiber breakage mechanism, and crack-healing efficiency, mechanical/fracture properties of BioFRC before MICP activation, and fracture properties enhancement of healed BioFRC.

CRediT authorship contribution statement

Mohammad Houshmand Khaneghahi: Conceptualization, Data curation, Formal analysis, Investigation, Methodology, Validation, Visualization, Writing – original draft, Writing – review & editing. **Seyed Ali Rahmaninezhad:** Methodology, Writing – review & editing. **Divya Kamireddi:** Methodology, Writing – review & editing. **Amirreza Sadighi:** Investigation, Writing – review & editing. **Christopher M. Sales:** Conceptualization, Funding acquisition, Project administration, Supervision, Writing – review & editing. **Caroline L. Schauer:** Conceptualization, Funding acquisition, Project administration, Supervision, Writing – review & editing. **Ahmad Najafi:** Conceptualization, Funding acquisition, Project administration, Supervision, Writing – review & editing. **Yaghoob (Amir) Farnam:** Conceptualization, Funding acquisition, Investigation, Project administration, Resources, Supervision, Validation, Writing – review & editing.

Declaration of competing interest

The authors declare that they have no known competing financial interests or personal relationships that could have appeared to influence the work reported in this paper.

Data availability

Data will be made available on request.

Acknowledgment

The work presented here has been supported by the National Science Foundation (NSF CMMI – 2029555) and was performed at Drexel University in the Advanced Infrastructure Materials (AIM) Lab. Any opinions, findings, and conclusions or recommendations expressed in this material are those of the authors and do not necessarily reflect the views of the National Science Foundation.

References

Amran, M., Onaizi, A.M., Fediuk, R., Vatin, N.I., Muhammad Rashid, R.S., Abdelgader, H., Ozbakkaloglu, T., 2022. Self-healing concrete as a prospective construction material: a review. Materials 15 (9), 3214.

Anbu, P., Kang, C.-H., Shin, Y.-J., So, J.-S., 2016. Formations of calcium carbonate minerals by bacteria and its multiple applications. SpringerPlus 5 (1), 1–26.

Azulay, D.N., Abbasi, R., Ben Simhon Ktorza, I., Remennik, S., Reddy, M.A., Chai, L., 2018. Biopolymers from a bacterial extracellular matrix affect the morphology and structure of calcium carbonate crystals. Cryst. Growth Des. 18 (9), 5582–5591.

Bekas, D., Tsirka, K., Baltzis, D., Paipetis, A.S., 2016. Self-healing materials: a review of advances in materials, evaluation, characterization and monitoring techniques. Compos. B Eng. 87, 92–119.

Bots, P., Benning, L.G., Rodriguez-Blanco, J.-D., Roncal-Herrero, T., Shaw, S., 2012. Mechanistic insights into the crystallization of amorphous calcium carbonate (ACC). Cryst. Growth Des. 12 (7), 3806–3814.

Castro-Alonso, M.J., Montañez-Hernandez, L.E., Sanchez-Muñoz, M.A., Macias Franco, M.R., Narayanasamy, R., Balagurusamy, N., 2019. Microbially induced calcium carbonate precipitation (MICP) and its potential in bioconcrete: microbiological and molecular concepts. Front. Mater. 6, 126.

Chan-u-tit, P., Laopaiboon, L., Jaisil, P., Laopaiboon, P., 2013. High level ethanol production by nitrogen and osmoprotectant supplementation under very high gravity fermentation conditions. Energies 6 (2), 884–899.

Chekroun, K.B., Rodríguez-Navarro, C., González-Muñoz, M.T., Arias, J.M., Cultrone, G., Rodríguez-Gallego, M., 2004. Precipitation and growth morphology of calcium carbonate induced by Myxococcus xanthus: implications for recognition of bacterial carbonates. J. Sediment. Res. 74 (6), 868–876.

Chen, L., Huang, L., Hua, J., Chen, Z., Wei, L., Osman, A.I., Yap, P.-S., 2023. Green construction for low-carbon cities: a review. Environ. Chem. Lett. 1–31.

Daminabo, S.C., Goel, S., Grammatikos, S.A., Nezhad, H.Y., Thakur, V.K., 2020. Fused deposition modeling-based additive manufacturing (3D printing): techniques for polymer material systems. Mater. Today Chem. 16, 100248.

Dhami, N.K., Reddy, M.S., Mukherjee, A., 2013. Biomineralization of calcium carbonates and their engineered applications: a review. Front. Microbiol. 4, 314.

Dinnebier, R.E., Billinge, S.J., 2008. Powder Diffraction: Theory and Practice. Royal society of chemistry.

Döbelin, N., 2020. Validation of XRD phase quantification using semi-synthetic data. Powder Diffr. 35 (4), 262–275.

Doebelin, N., Kleeberg, R., 2015. Profex: a graphical user interface for the Rietveld refinement program BGMN. J. Appl. Crystallogr. 48 (5), 1573–1580.

El Falafli, S., Hassan, M., 2021. The impact of the use of smart materials on the environment. Int. J. Adv. Eng. Civil Res. 1 (2), 41–54.

Ferral-Pérez, H., Galicia-García, M., Alvarado-Tenorio, B., Izaguirre-Pompa, A., Aguirre-Ramírez, M., 2020. Novel method to achieve crystallinity of calcite by Bacillus subtilis in coupled and non-coupled calcium-carbon sources. Amb. Express 10, 1–10.

Gebru, K.A., Kidanemariam, T.G., Gebretinsae, H.K., 2021. Bio-cement production using microbially induced calcite precipitation (MICP) method: a review. Chem. Eng. Sci. 238, 116610.

Ghosh, S.K., 2009. Self-healing Materials: Fundamentals, Design Strategies, and Applications, vol. 18. Wiley Online Library.

Guimard, N.K., Oehlenschlaeger, K.K., Zhou, J., Hilf, S., Schmidt, F.G., Barner-Kowollik, C., 2012. Current trends in the field of self-healing materials. Macromol. Chem. Phys. 213 (2), 131–143.

Hammes, F., Boon, N., de Villiers, J., Verstraete, W., Siciliano, S.D., 2003. Strain-specific ureolytic microbial calcium carbonate precipitation. Appl. Environ. Microbiol. 69 (8), 4901–4909.

Hassan, U., Anwar, M.S., 2010. Reducing noise by repetition: introduction to signal averaging. Eur. J. Phys. 31 (3), 453.

Hill, R., 1991. Expanded use of the Rietveld method in studies of phase abundance in multiphase mixtures. Powder Diffr. 6 (2), 74–77.

Hoffmann, T.D., Reeksting, B.J., Gebhard, S., 2021. Bacteria-induced mineral precipitation: a mechanistic review. Microbiology 167 (4).

Jimoh, O.A., Ariffin, K.S., Hussin, H.B., Temitope, A.E., 2018. Synthesis of precipitated calcium carbonate: a review. Carbonates Evaporites 33, 331–346.

Khaneghahi, M.H., Kamireddi, D., Rahmaninezhad, S.A., Schauer, C.L., Sales, C.M., Najafi, A., Farnam, Y., 2023a. Development of a nature-inspired polymeric fiber (BioFiber) for advanced delivery of self-healing agents. Construct. Build. Mater. 408 https://doi.org/10.1016/j.conbuildmat.2023.133765.

Khaneghahi, M.H., Kamireddi, D., Rahmaninezhad, S.A., Schauer, C.L., Sales, C.M., Najafi, A., Farnam, Y., 2023b. Development of bio-inspired multi-functional polymeric-based fibers (BioFiber) for advanced delivery of bacterial-based self-healing agent in concrete. In: Paper Presented at the MATEC Web of Conferences.

Khaneghahi, M.H., Kamireddi, D., Rahmaninezhad, S.A., Schauer, C.L., Sales, C.M., Najafi, A., Farnam, Y.A., 2023c. Development of bio-inspired multi-functional polymeric-based fibers (BioFiber) for advanced delivery of bacterial-based self-healing agent in concrete. In: Paper Presented at the MATEC Web of Conferences.

Kitamura, M., 2001. Crystallization and transformation mechanism of calcium carbonate polymorphs and the effect of magnesium ion. J. Colloid Interface Sci. 236 (2), 318–327.

Li, L., Zheng, Q., Li, Z., Ashour, A., Han, B., 2019. Bacterial technology-enabled cementitious composites: a review. Compos. Struct. 225, 111170.

Li, W., Dong, B., Yang, Z., Xu, J., Chen, Q., Li, H., Jiang, Z., 2018. Recent advances in intrinsic self-healing cementitious materials. Adv. Mater. 30 (17), 1705679.

Li, W., Liu, L., Chen, W., Yu, L., Li, W., Yu, H., 2010. Calcium carbonate precipitation and crystal morphology induced by microbial carbonic anhydrase and other biological factors. Process Biochem. 45 (6), 1017–1021.

Lv, C., Tang, C.-S., Zhang, J.-Z., Pan, X.-H., Liu, H., 2023. Effects of calcium sources and magnesium ions on the mechanical behavior of MICP-treated calcareous sand: experimental evidence and precipitated crystal insights. Acta Geotechnica 18 (5), 2703–2717.

MacAdam, J., Jarvis, P., 2015. Water-formed scales and deposits: types, characteristics, and relevant industries. In: Mineral Scales and Deposits. Elsevier, pp. 3–23.

Macha, I.J., Ben-Nissan, B., 2018. Marine skeletons: towards hard tissue repair and regeneration. Mar. Drugs 16 (7), 225.

Maleki Dizaj, S., Sharifi, S., Ahmadian, E., Eftekhari, A., Adibkia, K., Lotfipour, F., 2019. An update on calcium carbonate nanoparticles as cancer drug/gene delivery system. Expet Opin. Drug Deliv. 16 (4), 331–345.

Manzo, E., Russo, F., Perri, E., 2013. Carbonate Deposition in Tufa Systems: Processes and Products.

Martin, G., Guggiari, M., Bravo, D., Zopfi, J., Cailleau, G., Aragno, M., Junier, P., 2012. Fungi, bacteria and soil pH: the oxalate–carbonate pathway as a model for metabolic interaction. Environ. Microbiol. 14 (11), 2960–2970.
Mitchell, A.C., Ferris, F.G., 2006. The influence of Bacillus pasteurii on the nucleation and growth of calcium carbonate. Geomicrobiol. J. 23 (3–4), 213–226.
Muhammad Mailafiya, M., Abubakar, K., Danmaigoro, A., Musa Chiroma, S., Bin Abdul Rahim, E., Aris Mohd Moklas, M., Abu Bakar Zakaria, Z., 2019. Cockle shell-derived calcium carbonate (aragonite) nanoparticles: a dynamite to nanomedicine. Appl. Sci. 9 (14), 2897.
Nawarathna, T.H.K., Nakashima, K., Kawasaki, S., 2019. Chitosan enhances calcium carbonate precipitation and solidification mediated by bacteria. Int. J. Biol. Macromol. 133, 867–874.
Nguyen, P.Q., Courchesne, N.M.D., Duraj-Thatte, A., Praveschotinunt, P., Joshi, N.S., 2018. Engineered living materials: prospects and challenges for using biological systems to direct the assembly of smart materials. Adv. Mater. 30 (19), 1704847.
Nielsen, S.D., Koren, K., Löbmann, K., Hinge, M., Scoma, A., Kjeldsen, K.U., Røy, H., 2020. Constraints on CaCO 3 precipitation in superabsorbent polymer by aerobic bacteria. Appl. Microbiol. Biotechnol. 104, 365–375.
Oral, Ç.M., Ercan, B., 2018. Influence of pH on morphology, size and polymorph of room temperature synthesized calcium carbonate particles. Powder Technol. 339, 781–788.
Ortega-Villamagua, E., Gudiño-Gomezjurado, M., Palma-Cando, A., 2020. Microbiologically induced carbonate precipitation in the restoration and conservation of cultural heritage materials. Molecules 25 (23), 5499.
Pichon, B.P., Bomans, P.H., Frederik, P.M., Sommerdijk, N.A., 2008. A quasi-time-resolved cryoTEM study of the nucleation of CaCO3 under Langmuir monolayers. J. Am. Chem. Soc. 130 (12), 4034–4040.
Pouget, E.M., Bomans, P.H., Goos, J.A., Frederik, P.M., de With, G., Sommerdijk, N.A., 2009. The initial stages of template-controlled CaCO3 formation revealed by cryo-TEM. Science 323 (5920), 1455–1458.
Preetham, R., Krishna, R.H., Chandraprabha, M., Sivaramakrishna, R., 2021. Self-healing bacterial cementitious composites. Self-Healing Smart Mater. Allied Appl. 123–151.
Qin, J., Qin, Q., Li, X., Xue, J., Wang, R., Zhang, Q., Gong, Y., 2021. Urea supply control in microbial carbonate precipitation to effectively fill pores of concrete. Construct. Build. Mater. 310, 125123.
Rahmaninezhad, S.A., Farnam, A.Y., Schauer, C.L., Raeisi Najafi, A., Sales, C.M., 2022a. Evaluation of Different Strategies for Efficient Sporulation and Germination of the MICP Bacterium Lysinibacillus Sphaericus Strain MB284 (ATCC 13805). bioRxiv, 2022.2009. 2015.508202.
Rahmaninezhad, S.A., Farnam, Y.A., Schauer, C.L., Raeisi Najafi, A., Sales, C.M., 2022b. Influence of Culturing Media Components on the Growth and Microbial Induced Calcium Carbonate Precipitation (MICP) Activity of Lysinibacillus Sphaericus. bioRxiv, 2022.2005. 2023.493178.
Raina, A., Haq, M.I.U., Javaid, M., Rab, S., Haleem, A., 2021. 4D Printing for Automotive Industry Applications. Journal of The Institution of Engineers, Series D, pp. 1–9.
Rodriguez-Navarro, C., Jimenez-Lopez, C., Rodriguez-Navarro, A., Gonzalez-Muñoz, M. T., Rodriguez-Gallego, M., 2007. Bacterially mediated mineralization of vaterite. Geochem. Cosmochim. Acta 71 (5), 1197–1213.
Sadighi, A., Maghami, E., Khaneghahi, M.H., Kamireddi, D., Rahmaninezhad, S.A., Farnam, Y.A., Najafi, A.R., 2023. Fracture analysis of multifunctional fiber-reinforced concrete using phase-field method. Int. J. Solid Struct. 283, 112493.
Saulat, H., Cao, M., Khan, M.M., Khan, M., Khan, M.M., Rehman, A., 2020. Preparation and applications of calcium carbonate whisker with a special focus on construction materials. Construct. Build. Mater. 236, 117613.
Scrivener, K., Snellings, R., Lothenbach, B., 2016. A Practical Guide to Microstructural Analysis of Cementitious Materials, vol. 540. Crc Press, Boca Raton, FL, USA.
Seifan, M., Sarabadani, Z., Berenjian, A., 2020. Development of an innovative urease-aided self-healing dental composite. Catalysts 10 (1), 84.
Shrestha, R., Cerna, K., Spanek, R., Bartak, D., Cernousek, T., Sevcu, A., 2022. The effect of low-pH concrete on microbial community development in bentonite suspensions as a model for microbial activity prediction in future nuclear waste repository. Sci. Total Environ. 808, 151861.
Siddique, R., Chahal, N.K., 2011. Effect of ureolytic bacteria on concrete properties. Construct. Build. Mater. 25 (10), 3791–3801.
Simon, P., Pompe, W., Gruner, D., Sturm, E., Ostermann, K., Matys, S., Rödel, G., 2022. Nested Formation of calcium carbonate polymorphs in a bacterial surface membrane with a graded nanoconfinement: an evolutionary strategy to ensure bacterial survival. ACS Biomater. Sci. Eng. 8 (2), 526–539.
Sohail, M.G., Al Disi, Z., Zouari, N., Al Nuaimi, N., Kahraman, R., Gencturk, B., Yildirim, Y., 2022. Bio self-healing concrete using MICP by an indigenous Bacillus cereus strain isolated from Qatari soil. Construct. Build. Mater. 328, 126943.
Song, X., Zhang, L., Cao, Y., Zhu, J., Luo, X., 2020. Effect of pH and temperatures on the fast precipitation vaterite particle size and polymorph stability without additives by steamed ammonia liquid waste. Powder Technol. 374, 263–273.
Szcześ, A., Czemierska, M., Jarosz-Wilkołazka, A., 2016. Calcium carbonate formation on mica supported extracellular polymeric substance produced by Rhodococcus opacus. J. Solid State Chem. 242, 212–221.
Szcześ, A., Czemierska, M., Jarosz-Wilkołazka, A., Magierek, E., Chibowski, E., Hołysz, L., 2018. Extracellular polymeric substance of Rhodococcus opacus bacteria effects on calcium carbonate formation. Physicochem. Probl. Miner. Process. 54 (1), 142–150.
Thenepalli, T., Jun, A.Y., Han, C., Ramakrishna, C., Ahn, J.W., 2015. A strategy of precipitated calcium carbonate (CaCO 3) fillers for enhancing the mechanical properties of polypropylene polymers. Kor. J. Chem. Eng. 32, 1009–1022.
Tocheva, E.I., Dekas, A.E., McGlynn, S.E., Morris, D., Orphan, V.J., Jensen, G.J., 2013. Polyphosphate storage during sporulation in the gram-negative bacterium Acetonema longum. J. Bacteriol. 195 (17), 3940–3946.
Toohey, K.S., Sottos, N.R., Lewis, J.A., Moore, J.S., White, S.R., 2007. Self-healing materials with microvascular networks. Nat. Mater. 6 (8), 581–585.
Van Paassen, L.A., 2009. Biogrout, Ground Improvement by Microbial Induced Carbonate Precipitation.
Vidallon, M.L.P., Yu, F., Teo, B.M.J.C.G., Design, 2020. Controlling the size and polymorphism of calcium carbonate hybrid particles using natural biopolymers. Cryst. Growth Des. 20 (2), 645–652.
Vijayan, P.P., Puglia, D., 2019. Biomimetic multifunctional materials: a review. Emerg. Mater. 2 (4), 391–415.
Wang, X., Li, X., Zhao, L., Li, M., Li, Y., Yang, W., Ren, J., 2021. Polypyrrole-doped conductive self-healing multifunctional composite hydrogels with a dual crosslinked network. Soft Matter 17 (36), 8363–8372.
Weiner, S., Dove, P.M., 2003. An overview of biomineralization processes and the problem of the vital effect. Rev. Mineral. Geochem. 54 (1), 1–29.
Wen, K., Li, Y., Amini, F., Li, L., 2020. Impact of bacteria and urease concentration on precipitation kinetics and crystal morphology of calcium carbonate. Acta Geotechnica 15, 17–27.
Xu, J., Wang, X., Wang, B., 2018. Biochemical process of ureolysis-based microbial CaCO3 precipitation and its application in self-healing concrete. Appl. Microbiol. Biotechnol. 102, 3121–3132.
Zafar, B., Campbell, J., Cooke, J., Skirtach, A.G., Volodkin, D., 2022. Modification of surfaces with vaterite CaCO3 particles. Micromachines 13 (3), 473.
Zhang, L.V., Nehdi, M.L., Suleiman, A.R., Allaf, M.M., Gan, M., Marani, A., Tuyan, M., 2021. Crack self-healing in bio-green concrete. Compos. B Eng. 227, 109397.
Zhang, W., Ju, Y., Zong, Y., Qi, H., Zhao, K., 2018. In situ real-time study on dynamics of microbially induced calcium carbonate precipitation at a single-cell level. Environ. Sci. Technol. 52 (16), 9266–9276.